Semiconductor Science and Technology

PAPER • **OPEN ACCESS**

Electrically-active defects in reduced and hydrogenated rutile TiO_2

To cite this article: Julie Bonkerud *et al* 2021 *Semicond. Sci. Technol.* **36** 014006

View the article online for updates and enhancements.

IOP ebooks™

Bringing together innovative digital publishing with leading authors from the global scientific community.

Start exploring the collection–download the first chapter of every title for free.

This content was downloaded from IP address 129.240.128.148 on 14/12/2020 at 16:27

OPEN ACCESS
IOP Publishing
Semiconductor Science and Technology
Semicond. Sci. Technol. **36** (2020) 014006 (8pp)
https://doi.org/10.1088/1361-6641/abc854

Electrically-active defects in reduced and hydrogenated rutile TiO_2

Julie Bonkerud[1], Christian Zimmermann[1], Frank Herklotz[2], Philip Michael Weiser[1], Christoph Seiffert[1], Espen Førdestrøm Verhoeven[1], Lasse Vines[1] and Eduard V Monakhov[1]

[1] University of Oslo, Physics Department/Centre for Materials Science and Nanotechnology, P.O. Box 1048, Blindern, Oslo N-0316, Norway
[2] Technische Universität Dresden, Institute of Applied Physics, 01062 Dresden, Germany

E-mail: julie.bonkerud@smn.uio.no

Received 21 August 2020, revised 28 October 2020
Accepted for publication 6 November 2020
Published 27 November 2020

Abstract

We report on electrically-active defects located between 0.054 and 0.69 eV below the conduction band edge in rutile TiO_2 single crystals subjected to reducing and hydrogenating heat treatments. Deep-level transient spectroscopy measurements recorded on TiO_2 samples subjected to different heat treatments are compared. In samples annealed in H_2 gas, three defect levels are commonly observed. One of these levels, E_{192}, located 0.43 eV below the conduction band edge is tentatively assigned to a hydrogen-impurity complex. Two levels at 0.054 and 0.087 eV below the conduction band edge, which were present after all different heat treatments, are tentatively assigned as being related to O vacancies or Ti self-interstitials. Deep-level transient spectroscopy spectra of samples heat-treated in N_2 display a larger number of defect levels and larger concentrations compared to samples heat-treated in H_2 gas. N_2 treatments are performed at considerably higher temperatures. Four energy levels located between 0.28 and 0.69 eV, induced by annealing in N_2, are tentatively attributed to O vacancy- or Ti interstitial-related complexes with impurities.

Keywords: defects in semiconductors, deep-level transient spectroscopy, TiO_2, deep-level transient spectroscopy, rutile

(Some figures may appear in colour only in the online journal)

1. Introduction

Rutile titanium dioxide (TiO_2) is a wide bandgap semiconductor ($E_g = 3.2$ eV [1–4]) that is well-known for its photocatalytic properties [5, 6], enabling applications such as photocatalytic water-splitting and water purification [6–10]. Reduced and/or hydrogenated TiO_2 (TiO_{2-x}:H) has gained interest because it displays enhanced photocatalytic activity [11–13]. The photocatalytic performance of TiO_2 can be improved further by the presence of defects that promote the transfer of charges to reactive species [1, 14]. Additionally, defects can extend the optical absorption of TiO_2 into the visible part of the electromagnetic spectrum [15–17]. Recently, Nitta *et al* identified a correlation between the photocatalytic performance of certain TiO_2 powders and the energy distribution of shallow electron traps [9, 18]. For TiO_{2-x}:H, hydrogen (H) and intrinsic defects whose formation is favourable under reducing conditions, such as oxygen vacancies and and Ti self-interstitials [16, 19], can be expected to play a key role.

In applications, TiO_2 is usually used in the form of powders or nano-crystals [9, 18], making fundamental studies concerning the electronic properties of defects in the materials challenging. In contrast, single-crystalline TiO_2 can function as a model system for defect studies. Particularly, single crystals

Original Content from this work may be used under the terms of the Creative Commons Attribution 4.0 licence. Any further distribution of this work must maintain attribution to the author(s) and the title of the work, journal citation and DOI.

which have been subjected to hydrogenating and/or reducing heat treatments might display a defect chemistry comparable to the one found in TiO_2 used for photocatalysis, and are therefore important to study.

Deep-level transient spectroscopy (DLTS) is a powerful method for investigation of electrically-active defects [20]. However, reports regarding DLTS on defects in TiO_2 are scarce [21–23]. One reason for this is the challenge of fabricating high quality Schottky barrier diodes (SBDs) on TiO_2. In our recent paper, we have shown that Schottky barrier diodes between Pd and TiO_{2-x}:H suitable for space-charge spectroscopy can be fabricated [24]. Using DLTS, we identified several defect-related charge state transition levels in TiO_{2-x}:H [23], but no clear assignments to certain defects have so far been made. The heat treatments consisted of anneals in either closed ampoules filled with H_2 gas or in flowing gas, such as forming gas (FG) or N_2. Three defect energy levels with positions of about 0.070, 0.095, and 0.12 eV below the conduction band edge, E_c, occurred in all the studied samples, irrespective of the sample production batch and the heat treatment used. In samples annealed in FG flow, seven distinct levels in the range 0.057–0.63 eV were detected. In samples annealed in H_2 gas, four distinct levels in the range 0.049–0.47 eV were detected. In samples annealed in N_2 flow, six distinct levels in the range 0.063–0.40 eV were detected. No defect with a charge state transition level in the 0.20–0.70 eV range below E_c was present after all of the different heat treatments, indicating a strong influence on deep-level defects by the post-growth heat treatments employed [23].

The present paper aims to further investigate electrically-active defects in TiO_2 single crystals subjected to reducing and/or hydrogenating heat treatments. Here, we extend the previous study to different annealing temperatures and durations, and follow the evolution of different defects. This data are crucial for identification of the defects. Additionally, the paper examines the role of H in electrically-active defects in TiO_2. The interstitial hydrogen concentration, $[H_i]$, of crystals annealed in H_2 gas, is deduced from Fourier-Transform infrared spectroscopy measurements, prior to electrical measurements. The correlation between $[H_i]$ and transition level concentrations is investigated.

2. Experimental

2.1. Samples

The study described here was performed on float-zone (FZ) grown rutile TiO_2 single crystals with a surface orientation of (001), purchased from *MTI Corporation* [25]. As-received crystals were 0.5 mm thick, nominally undoped, transparent, and semi-insulating with a conductivity of $\sigma < 10^{-7}\,\Omega^{-1}\,cm^{-1}$. Doping by heat treatments was necessary to perform electrical measurements on the TiO_2 single crystals. Conductive *n*-type TiO_2 single crystals are known to display a bluish color [26–32]. Conductive *n*-type TiO_2 samples of bluish colour was obtained by heat treatments in hydrogenating and/or reducing atmospheres [23, 24]. Hydrogen was introduced either by annealing in FG flow (N_2 + H_2 with $[H_2]\,/\,[N_2] \approx 1/9$) at 600–740 °C for 25–90 min or by annealing in closed ampoules filled with approximately 0.5 bar of H_2 gas at 400–600 °C for 10–60 min. Additionally, samples were annealed in N_2 flow for 1–25 h. Samples heat treated in N_2 flow were annealed at the same time in the furnace, but were exposed to different temperatures in the range 900–1200 °C due to their different locations inside the furnace. For the N_2-annealed samples the temperatures were determined to 900 °C, 1050 °C and 1200 °C within ±30 °C by measuring the temperature-profile of the furnace with a thermocouple element. In the following, the crystals are labelled according to their heat treatment; TiO_2-N_2 (annealed in N_2 flow), TiO_2-FG (annealed in FG flow) and TiO_2-H_2 (annealed in closed ampoules with H_2 gas). The samples are labelled according to their annealing temperature (T_{anneal}) and annealing duration (t_{anneal}), for example, *450 C-60 min*.

In order to have a reference sample that had not been heat-treated, rutile TiO_2 single crystals doped with 0.01 wt% of Nb were purchased from *Shinkosha* [33]. These crystals were 0.5 mm thick with a surface orientation of (001), and were grown by the Verneuil (V) method. The as-received TiO_2-Nb crystals exhibited *n*-type conductivity and a bluish color, with a conductivity of $0.048\,\Omega^{-1}\,cm^{-1}$. The Nb-doped sample is denoted as TiO_2-Nb.

Schottky barrier diodes (SBDs) were obtained by e-beam evaporation of 150 nm Pd on the (001) surface of the TiO_2 crystals [24]. The Pd contacts were deposited using Si or Al shadow masks with typical diameters between 300 and 500 μm. InGa or Ti/Al was used as Ohmic back contact. Characterization of the crystals and the SBDs are described in detail elsewhere [24].

2.2. Experimental set-up

The electrical conductivity, σ, of TiO_2 single crystals was determined by using a four-point probe measurement according to the van-der-Pauw method [34, 35]. The measurement utilized a Keithley 7001 switching system, a Keithley 2182A nano-volt-meter and a Keithley 6221 current source. Eutectic InGa pads were used as Ohmic contacts in the corners of the samples.

Fourier-Transform infrared (FT-IR) spectroscopy was used to determine $[H_i]$ in TiO_2 single crystals prior to metal contact deposition. Infrared (IR) transmittance spectra were measured using an evacuated Bruker IFS 125HR spectrometer equipped with a globar light source, a KBr beamsplitter, and a liquid-nitrogen-cooled InSb detector. The IR beam was kept at normal incidence ($\pm 3^{\circ}$) with respect to the (001) surface of the TiO_2 single crystals. Measurements were performed at room temperature using a spectral resolution of 1 cm^{-1}. $[H_i]$ was determined from the integrated area of the optical absorption associated with the stretch O–H local vibrational mode (LVM) of H_i at about 3278 cm^{-1} [36] using a calibration factor determined by Johnson *et al* [37].

Secondary ion mass spectrometry (SIMS) measurements were performed using a Cameca IMS 7f instrument with a primary beam of 10 keV O^{2+} ions. Rutile TiO_2 samples implanted with Cr, Al, Si or Fe were used as references to

obtain absolute concentration values. For other residual elements, relative concentrations were determined. A constant erosion rate was assumed for depth-calibration, where the crater depths were measured using a surface Stylus Profilometer.

Capacitance-voltage (CV) measurements were carried out at room temperature using an Agilent 4284A LCR meter or a Boonton 7200 capacitance meter, respectively. The donor concentration, N_d, was deduced from CV measurements, using the depletion approximation [38], a probing frequency of $f_{meas} = 1$ MHz, and assuming a value of $\epsilon_{TiO_2} = 160$ at room temperature for the static relative dielectric constant of TiO_2 [39, 40].

DLTS was conducted using a refined version of the setup described elsewhere [41], which utilizes a Boonton 7200 capacitance meter and a closed-cycle He cryostat. During measurements, reverse bias voltages between -6 V and -2 V were applied. Filling pulses with an amplitude of 2–6 V and a duration of 50 ms were employed. The DLTS signal was extracted from the acquired capacitance versus time transients using a lock-in weighting function with six different rate windows in the range from $(20\,\text{ms})^{-1}$ to $(640\,\text{ms})^{-1}$ or a GS-4 weighting function with five different rate windows in the range of $(40\,\text{ms})^{-1}$ to $(640\,\text{ms})^{-1}$ [20, 42, 43]. A delay time of 5 ms and a temperature (T) resolution of 0.5–1 K were used. Measurements were performed during heat-up in the temperature range 20–300 K. The apparent capture cross-section, σ_{ap}, and the thermal activation energy, E_A, for the deep-level defects were deduced from simulating the DLTS spectra as described in detail in [44]. The peaks in the DLTS spectra are labelled after the peak temperature position of the longest time window measured (rate window $[640\,\text{ms}]^{-1}$). The defect concentration, N, can be deduced from the DLTS signal, assuming a uniform and sufficiently low $\leq 0.1N_d$ defect distribution, where [20].

$$N = 2\frac{\Delta C}{C_{rb}}N_d. \quad (1)$$

Here, ΔC is the amplitude of the measured capacitance transients [20, 42], while C_{rb} is the steady-state reverse bias capacitance.

3. Results

3.1. Impurities and interstitial hydrogen concentration

The impurity content of TiO_2 crystals was investigated with SIMS. A typical mass spectrum of a conductive TiO_2 crystal is shown in figure 1(a). The measurements reveal that Al, Si, Cr and Fe are present in the crystals. It should be noted that the mass spectrum shown in figure 1(a) is not a direct measurement of impurity concentrations because the count rates depend on both the concentration and the ionization probability of an impurity. In order to deduce the concentrations, one has to measure a calibration sample with known impurity concentrations. For the sample for which data are shown in figure 1(a), the measured impurity concentrations were $[Si] \simeq 1 \times 10^{17}\,\text{cm}^3$, $[Al] \simeq 2 \times 10^{15}\,\text{cm}^3$, $[Cr] \simeq 8 \times 10^{15}\,\text{cm}^3$ and $[Fe] \simeq 5 \times 10^{17}\,\text{cm}^3$. The SIMS measurements did not reveal any significant influence of the annealing on the impurity concentrations. Detection of H by SIMS is difficult due to the high background concentration, and it was not possible to deduce [H] from SIMS measurements on as-received or heat-treated crystals.

Heat treatments in H_2 gas, FG flow or N_2 flow led to TiO_2 single crystals with a bluish color and n-type conductivity in the range from $(0.5 - 8) \times 10^{-2}\,\Omega^{-1}\,\text{cm}^{-1}$.

Figure 1(b) shows IR absorption coefficient spectra of the $3278\,\text{cm}^{-1}$ H_i LVM for as-received and heat-treated samples. Data are shown for the wavenumber region where optical absorption associated with a local vibrational mode of H_i can be seen [36]. In the as-received, nominally undoped crystals, $[H_i]$ is typically in the lower range of 10^{17} cm^{-3}. After heat treatments in FG flow or H_2 gas, $[H_i]$ increases by an order of magnitude or more, whereas crystals annealed in N_2 flow display decreased $[H_i]$ compared to the $[H_i]$ in as-received TiO_2 crystals. Interstitial hydrogen is reported to be a shallow donor in rutile TiO_2 [36, 45, 46]. Strong indications of H_i being the main donor in TiO_2-FG and TiO_2-H_2 crystals are given in reference [47], in form of a linear correlation between σ and $[H_i]$ over a range of one order of magnitude. After hydrogenation, $[H_i]$ remains stable. No change in the $[H_i]$ of the samples was observed over the course of a few months when storing the samples at around $-20\,^\circ$C. IR absorption coefficient spectra for the *400 C-60 min* sample annealed in H_2 gas, recorded immediately after heat treatment and three months later, are shown in figure 1(b). The difference between the spectra is smaller than the measurement uncertainty.

$[H_i]$ was measured to be $1.8 \times 10^{16}\,\text{cm}^{-3}$ in the as-received TiO_2-Nb crystal, which is an order of magnitude lower than $[H_i]$ in the as-received, nominally undoped crystals.

3.2. Energy levels present in heat-treated crystals

3.2.1. TiO_2-H_2 crystals. Figure 2 shows DLTS spectra recorded on SBDs comprising different TiO_2-H_2 samples. The annealing of crystals in closed ampoules with H_2 gas performed at 450 °C resulted in $[H_i]$ from $1.6 \times 10^{18}\,\text{cm}^{-3}$ to $3.1 \times 10^{18}\,\text{cm}^{-3}$. The IR spectrum of the H_i vibrational line in *450 C-60 min* sample is shown in figure 1(b). For the most conductive sample, which was annealed at 600 °C for 10 min, the strong absorption due to charge carriers masks the OH spectral region, and prevents quantitative evaluation of $[H_i]$. For this sample, $[H_i]$ was estimated to be $8.9 \times 10^{18}\,\text{cm}^{-3}$ from its value for σ, assuming that the linear relationship between $[H_i]$ and σ holds [47]. All DLTS spectra of TiO_2-H_2 samples display three defect levels; two shallow levels located around 0.087 and 0.11 eV below E_c (E_{40} and E_{55}), and a level located at 0.43 eV below E_c (E_{192}). Measurements using different reverse biases do not reveal Poole-Frenkel effect for E_{40}, E_{55} and E_{192}, which suggests acceptor nature. These levels correspond to $E_{3,H2}$, $E_{4,H2}$ and $E_{5,H2}$ reported in our previous paper [23].

E_{192} is the dominating peak in the TiO_2-H_2 samples. $[E_{192}]$ is in the range of $2 \times 10^{15}\text{cm}^{-3}$ to $2 \times 10^{16}\,\text{cm}^{-3}$, one order of magnitude larger than the concentrations of the shallow levels present in the same spectra. A comparison of the three

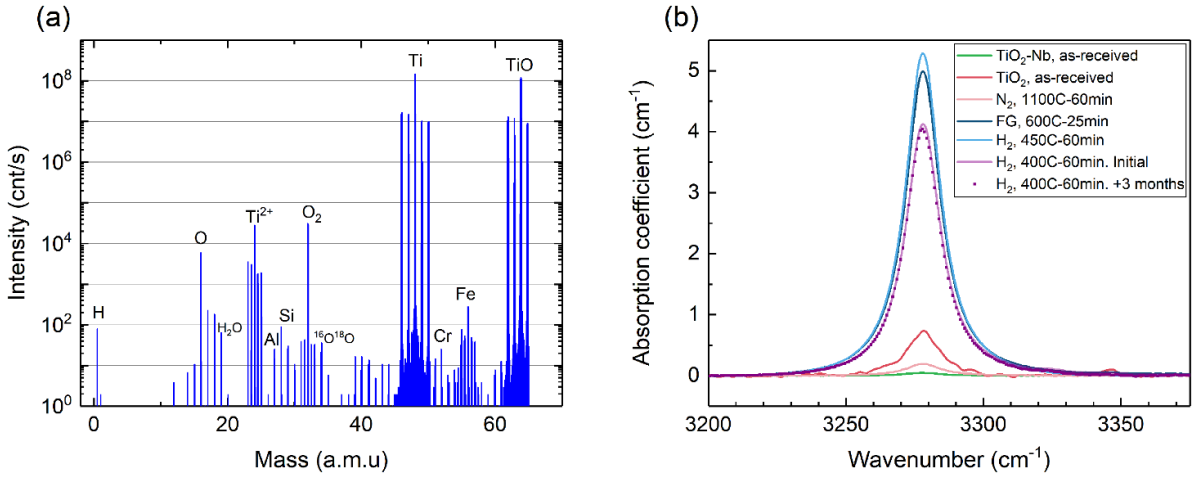

Figure 1. (a) Mass spectrum of a conductive TiO_2 crystal used in the study. (b) Infrared absorption spectra of the 3278 cm^{-1} H_i vibrational line for as-received crystals (semi insulating and Nb-doped), and after annealing in different environments (H_2, N_2 or FG).

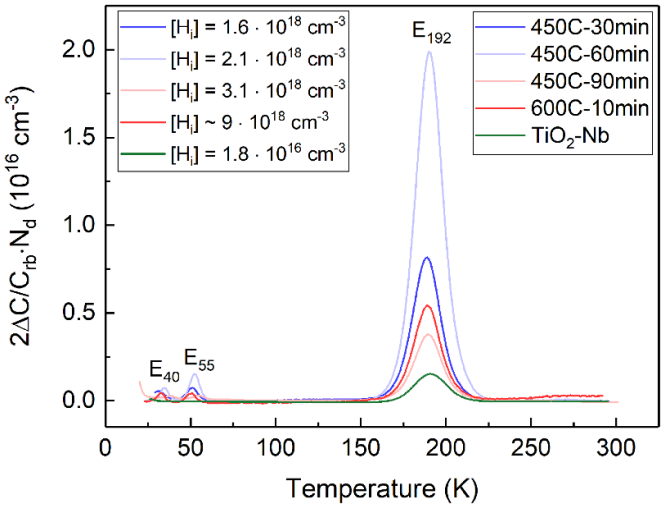

Figure 2. DLTS spectra recorded on TiO_2-H_2 samples annealed at 450 °C or 600 °C for different durations, and a TiO_2-Nb sample. DLTS spectra were constructed using a lock-in weighting function with rate window $(640\,\text{ms})^{-1}$. TiO_2-H_2 samples display a varying concentration of H_i in the order of 10^{18} cm^{-3}, while the Nb-doped sample reveals $[H_i] = 1.8 \times 10^{16}\,cm^{-3}$.

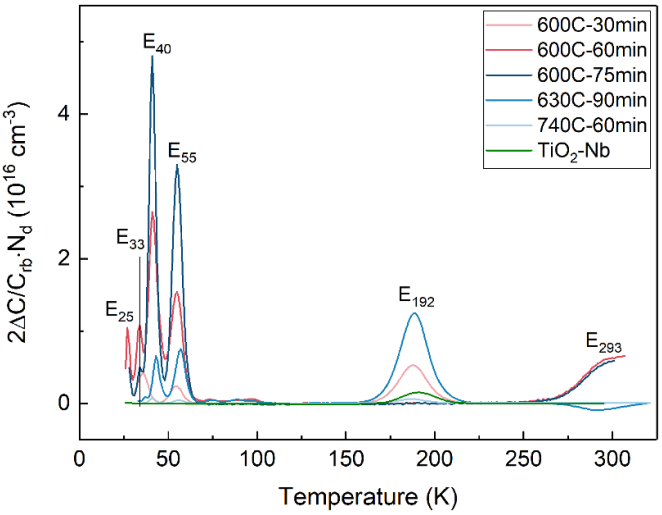

Figure 3. DLTS spectra recorded on samples annealed in FG flow at 600–740 °C for 30–90 min, and a TiO_2-Nb sample. DLTS spectra were constructed using a lock-in weighting function with rate window $(640\,\text{ms})^{-1}$.

samples that were annealed at 450 °C for different durations, shows that $[H_i]$ and N_d both increase with annealing time. However, the corresponding DLTS spectra do not display a similar dependence. The DLTS spectrum recorded for the sample annealed at 600 °C, with significantly larger $[H_i]$, display DLTS peaks with similar amplitudes compared to those in spectra recorded for samples annealed at 450 °C.

3.2.2. TiO_2-FG crystals. Similar to the hydrogenating treatment in closed ampoules filled with H_2 gas, the forming gas heat treatment also increases the $[H_i]$ compared to that of the as-grown crystal (figure 1(b)). Annealing in FG, however, requires higher temperatures and/or longer annealing times for achieving sufficiently conductive crystals for junction spectroscopy. For instance, annealing of a crystal in H_2 gas at 600 °C for 10 min was sufficient in order to fabricate suitable SBDs. In comparison, TiO_2-FG crystals required an annealing duration in the order of 1 h to achieve conductive crystals and to fabricate suitable SBDs [24]. This is corroborated by comparing FT-IR spectra shown in figure 1. $[H_i]$ is similar for the TiO_2-H_2 sample annealed at 450 °C for 60 min and the TiO_2-FG sample annealed at 600 °C for 25 min. Therefore, TiO_2-FG samples are expected to be more heavily reduced, compared to TiO_2-H_2 samples, and other defects may appear, that were not present in TiO_2-H_2 samples. Another major difference between the annealing procedures in FG flow and H_2 gas is the cooling process afterwards. While the TiO_2-H_2 samples were allowed to cool down inside the ampoule until they reached room temperature, FG annealed samples were quenched in air, or cooled down in flowing gas, placed at the cooler part of the annealing tube. The exposure to air at elevated temperatures might lead

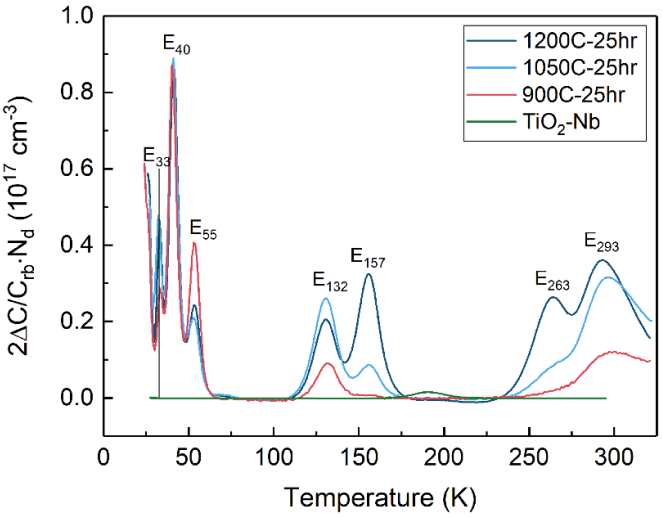

Figure 4. DLTS spectra recorded on samples annealed in N_2 flow at different temperatures for 25 h, and a TiO_2-Nb sample. DLTS spectra were constructed using a lock-in weighting function with rate window $(640\,\mathrm{ms})^{-1}$.

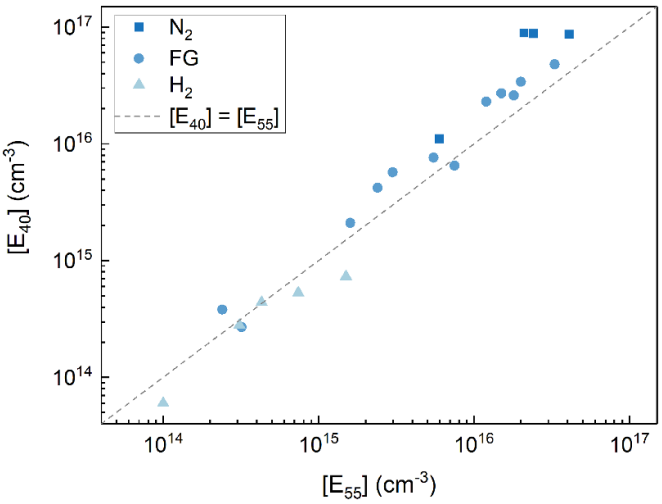

Figure 5. $[E_{40}]$ as a function of $[E_{55}]$ for samples annealed in H_2 gas, FG flow or N_2 flow.

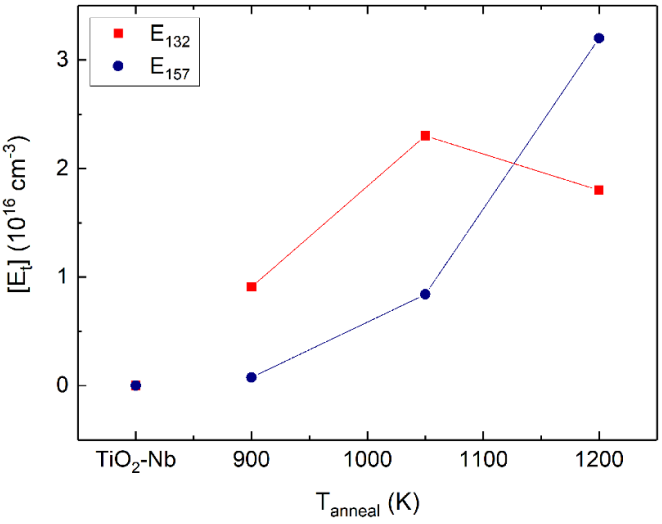

Figure 6. Dependence of $[E_{132}]$ and $[E_{157}]$ on T_{anneal} for samples annealed in N_2 flow for 25 h.

to the creation of different defects, out-diffusion of defects, or out-diffusion of H.

Compared to TiO_2-H_2, the DLTS spectra for TiO_2-FG samples show a wider variation in both the number of peaks and their amplitudes, as is shown in figure 3. For example, the three levels present in TiO_2-H_2 (E_{40}, E_{55}, and E_{192}) are also present in TiO_2-FG samples, but now E_{40} and E_{55} are the dominant levels. A large variation in defect concentrations is observed. $[E_{33}]$, $[E_{40}]$ and $[E_{55}]$ are in the range 3×10^{14} to $5 \times 10^{16}\,\mathrm{cm}^{-3}$, while $[E_{192}]$ varies from $< 5 \times 10^{13}\,\mathrm{cm}^{-3}$ to $1 \times 10^{16}\,\mathrm{cm}^{-3}$. These concentrations do not vary systematically with annealing time or temperature. Other defect levels are observed occasionally, such as E_{25} and E_{293}. E_{293} is observed in DLTS spectra from the *600 C-60 min* and *600 C-75 min* samples, shown in figure 3. These samples originate from the same wafer.

3.2.3. TiO_2-N_2 crystals. Figure 4 shows DLTS spectra of different samples annealed in N_2 flow at 900 °C–1200 °C for 25 h. Compared to the DLTS spectra for the hydrogenated samples shown in figure 2 and figure 3, several other defect levels are present; E_{132}, E_{157} and E_{263}. Similarly to TiO_2-H_2 and TiO_2-FG, several shallow levels are present in the low temperature region; E_{33}, E_{40} and E_{55}. An additional level appears at very low temperatures with a large peak, which is out of the temperature range of the measurements. $[E_{33}]$, $[E_{40}]$ and $[E_{55}]$ in TiO_2-N_2 samples are approximately two orders of magnitude larger than in the TiO_2-H_2 samples.

E_{132} and E_{157} correspond to $E_{5,N}$ and $E_{6,N}$ previously detected in FZ-grown TiO_2-N_2 [23]. The three TiO_2-N_2 samples in figure 4 (*1200 C–25 hr*, *1050 C–25 hr* and *900 C–25 hr*) originate from a single wafer.

The annealing data reveal an intricate formation kinetics for E_{132} and E_{157}. E_{132} appears in the sample annealed at 900 °C, and has a higher concentration in the sample annealed at 1050 °C. However, an increased T_{anneal} of 1200 °C results in a lower concentration. In contrast, E_{157} hardly appears in the sample annealed at 900 °C, but shows a strong growth with increasing T_{anneal}. E_{293} and E_{263} demonstrate a similar behaviour as E_{132} and E_{157}: E_{293} is present in the sample annealed at lower T_{anneal}, but $[E_{293}]$ nearly stabilizes for $T_{\mathrm{anneal}} > 1050$ ° C. E_{263}, on the other hand, shows a strong growth with increasing T_{anneal}, similar to E_{157}.

4. Discussion

4.1. Shallow levels

Four DLTS peaks are visible in the temperature region 25–55 K. E_{25}, observed in some DLTS spectra recorded on TiO_2-FG samples, appears at very low temperatures and was not resolved for all the measurements performed. E_{33} is observed

Table 1. Defect levels present in rutile TiO_2 samples. Activation energy, E_A, and apparent capture cross-section, σ_{ap}, were deduced from simulations of DLTS spectra [44]. The uncertainties of E_A and σ_{ap} is around 10% and one order of magnitude, respectively.

			Observed in crystal				
Level	E_A (eV)	σ_{ap} (cm^2)	N_2	FG	H_2	Nb	Tentative assignment
E_{33}	0.054	4×10^{-17}	✓	✓			V_O- and/or Ti_i-related
E_{40}	0.087	7×10^{-15}	✓	✓	✓		V_O- and/or Ti_i-related
E_{55}	0.11	9×10^{-16}	✓	✓	✓		V_O- and/or Ti_i-related
E_{132}	0.28	4×10^{-16}	✓				V_O- and/or Ti_i-related
E_{157}	0.38	9×10^{-15}	✓				V_O- and/or Ti_i-related
E_{192}	0.43	1×10^{-15}		✓	✓	✓	A-H, A = Al, Cr, Si, or Fe
E_{263}	0.63	2×10^{-15}	✓				V_O- and/or Ti_i-related
E_{293}	0.69	2×10^{-15}	✓	✓			V_O- and/or Ti_i-related

in all the TiO_2-N_2 samples, but only in some of the TiO_2-FG samples. Furthermore, $[E_{33}]$ is higher in TiO_2-N_2 samples compared to TiO_2-FG samples. E_{40} and E_{55} are detected in all heat-treated samples regardless of the type of heat treatment, but were not present in DLTS spectra recorded on TiO_2-Nb samples. Interestingly, E_{40} and E_{55} always appear together in DLTS spectra. This correlation can be seen in figure 5, where $[E_{40}]$ is plotted vs. $[E_{55}]$ for all of the different heat treatments. The plot reveals a significant correlation over almost three orders of magnitude between $[E_{40}]$ and $[E_{55}]$, with a correlation coefficient close to one. The independence of this correlation on the exact heat treatment suggests that E_{40} and E_{55} originate from the same defect. The two levels can be either different charge-state transition levels of the same defect or inequivalent configurations of the same defect. Such a correlation was not observed between E_{33} and E_{40}, or between E_{33} and E_{55}. Furthermore, the data in figure 5 show that the type of heat treatment affects the concentrations of E_{40} and E_{55}. $[E_{40}]$ and $[E_{55}]$ vary over more than two orders of magnitude in TiO_2-FG samples, from $2 \times 10^{14}\,cm^{-3}$ to $5 \times 10^{16}\,cm^{-3}$. In contrast, $[E_{40}]$ and $[E_{55}]$ are lower (in the order of 10^{14} cm^{-3}) in TiO_2-H_2 samples, whereas they are higher (in the order of 10^{16} cm^{-3}) in TiO_2-N_2 samples. As mentioned above, all the heat treatments can result in reduction of TiO_2, which promotes the formation of oxygen vacancies (V_O) and Ti self-interstitials (Ti_i) [16, 19, 48–52]. However, the anneals in FG and N_2 are expected to have a stronger effect because of the higher annealing temperatures. Since $[E_{33}]$, $[E_{40}]$, and $[E_{55}]$ are higher for these treatments, we attribute E_{33}, E_{40} and E_{55} to V_O- and/or Ti_i-related defects.

4.2. Deep levels

The E_{192} level was previously detected in TiO_2 samples heat-treated in H_2 gas or FG flow (reported as $E_{5,H2}$ and $E_{7,FG}$ in our previous paper [23]), but not in samples annealed in N_2. We observe that E_{192} responds to heat treatments in H_2, and, therefore, can be tentatively attributed to a H-related defect. On the other hand, the absence of strong correlation between $[E_{192}]$ and the conditions of treatment (figure 2) indicates that the level does not originate from a defect that contains only H. For instance, E_{192} could originate from a defect complex between H and another impurity. In this case, the concentration of the other impurity will limit the concentration of E_{192} observed by DLTS. $[E_{192}]$ is in the range of $0.5–2 \times 10^{16}\,cm^{-3}$, which is comparable to the concentration of residual impurities determined by SIMS (figure 1(a)), but considerably lower than the $[H_i]$ in the order of 10^{18} cm^{-3} determined by FT-IR (figure 1(b)). Some variation in impurity concentrations among the samples can be expected, which can explain the variations in $[E_{192}]$ for different samples. Hence, we attribute E_{192} to a hydrogen-impurity complex, that we denote as A-H, where A = Si, Al, Cr, or Fe.

We observe only a single level, E_{192}, at higher temperatures for both TiO_2-FG and TiO_2-H_2 samples, as well as TiO_2-Nb. This level coincides with the level of an electron trap reported by Duckworth *et al* in Nb-doped rutile TiO_2 single crystals, who reported an activation energy of 0.38 eV for this peak [22]. We determined a slightly higher activation energy of 0.43 eV for this level. However, variations between different samples are observed when calculating E_A [23]. The value for the energy level reported by Duckworth *et al* falls within the range of E_A that we determine, taking into account fitting errors and the scatter between the measured samples [23]. Duckworth *et al* estimated σ_{ap} to be $3 \times 10^{-16}\,cm^2$ [22], which is one order of magnitude larger than $\sigma_{ap,192}$ deduced here (see table 1). Duckworth *et al* also reported two small features on the low temperature side of the main peak in the DLTS spectrum. There is no indication of several contributions to the E_{192} peak in the DLTS spectra shown in figure 2 or figure 3. Furthermore, analysis of the data using the GS4 weighting function [43], which provides a better energy resolution than the lock-in weighting function, did not reveal any additional contributions to this peak.

As mentioned in previous sections, the recorded concentrations of E_{132}, E_{157}, E_{263}, and E_{293} indicate that the levels have an intricate formation kinetics. For example, for the data shown in figure 4, E_{132} starts to grow prior to E_{157}, and stabilizes or even decrease at higher temperatures. In contrast, E_{157} starts to grow after E_{132}, and $[E_{157}]$ increases monotonically with temperature. The dependence of $[E_{132}]$ and $[E_{157}]$ on annealing temperature is shown in figure 6. Such a behaviour can be explained if E_{132} is a precursor for E_{157}. Besides, E_{132} and E_{157} have electronic levels close to each other, which may indicate their similar nature. We observe formation of E_{132} and E_{157} after N_2 treatment at ∼1000 °C, which is expected to

introduce V_O and Ti_i. Thus, both E_{132} and E_{157} can be tentatively attributed to V_O- or Ti_i-related defects. One can put forward the following speculation of the formation kinetics:

$$E_{132} : X + V_O(Ti_i) \rightarrow X\text{-}V_O(Ti_i) \quad (2)$$

$$E_{157} : X\text{-}V_O(Ti_i) + V_O(Ti_i) \rightarrow X\text{-}V_{O2}(Ti_{i2}), \quad (3)$$

where X is an impurity. Similar considerations can be put forward for E_{263} and E_{293}.

In table 1, the activation energy determined by DLTS, the apparent capture cross-section and tentative assignments, are summarized. E_A is the activation energy for thermally-induced electron emission from a defect, and is the sum of the single thermodynamic charge-state transition level, E_t, and the corresponding energetic barrier for electron capture [34, 53].

5. Conclusion

The effect of annealing temperature on electrically-active defects in single-crystalline rutile TiO_2 was investigated by annealing nominally undoped TiO_2 in H_2 gas, FG flow, or N_2 flow. DLTS spectra recorded after different heat treatments were compared to the DLTS spectrum of a Nb-doped reference sample that had not been annealed. The spectra recorded on the reference sample display a single peak, E_{192}. This peak responds to treatment in H_2, but does not directly follow the $[H_i]$ determined from IR measurements. Therefore, we tentatively assign E_{192} to an impurity-hydrogen complex, denoted A-H, where A = Si, Al, Cr, or Fe.

In spectra recorded on heat-treated samples, the two levels E_{40} and E_{55} are commonly observed regardless of the type of heat treatment. A strong correlation between $[E_{40}]$ and $[E_{55}]$ demonstrates that the two levels are related to either different charge states of the same defect or different structural configurations of the same defect. Since E_{40} and E_{55} respond to reducing heat treatments, they are attributed to V_O- and/or Ti_i-related defects.

Four additional charge state transition levels, E_{132}, E_{157}, E_{263} and E_{293}, located between 0.28 eV and 0.69 eV below E_c, are induced by annealing in N_2. These levels are tentatively attributed to V_O- or Ti_i-related defects. Their formation kinetics seem to suggest E_{132} and E_{293} being precursors to E_{157} and E_{263}, respectively.

Acknowledgments

The Research Council of Norway is acknowledged for the support to the Norwegian Micro- and Nano-Fabrication Facility, NorFab, PROJECT NUMBER 245963. Financial support by the Research Council of Norway via the EEA-JRP-RO-NO-2013-1 European Project (PERPHECT), the Research Center for Sustainable Solar Cell Technology (FME SUSOLTECH, project number 257639), and the Norwegian PhD Network on Nanotechnology for Microsystems (project number 221860/F60), is gratefully acknowledged. Financial support by the Faculty of Mathematics and Natural Sciences at the University of Oslo via the strategic research initiative FOX-HOUND is gratefully acknowledged.

ORCID iDs

Julie Bonkerud https://orcid.org/0000-0001-8353-9842
Christian Zimmermann https://orcid.org/0000-0003-3708-6074
Lasse Vines https://orcid.org/0000-0001-5759-7192

References

[1] Nowotny M K, Bak T and Nowotny J 2006 *J. Phys. Chem.* B **110** 16270
[2] Vos K 1977 *J. Phys. C: Solid State Phys.* **10** 3917
[3] Vos K and Krusemeyer H 1974 *Solid State Commun.* **15** 949
[4] Pascual J, Camassel J and Mathieu H 1978 *Phys. Rev.* B **18** 5606
[5] Ni M, Leung M, Leung D and Sumathy K 2007 *Renew. Sust. Energy. Rev.* **11** 401
[6] Fujishima A, Zhang X and Tryk D 2008 *Surf. Sci. Rep.* **63** 515
[7] Carp O, Huisman C and Reller A 2004 *Prog. Solid State Chem.* **32** 33
[8] Cong Y, Zhang J, Chen F and Anpo M 2007 *J. Phys. Chem* **111** 6976
[9] Nitta A, Takashima M, Takase M and Ohtani B 2019 *Catal. Today* **321** 2
[10] Hoffmann M R, Martin S T, Choi W and Bahnemann D W 1995 *Chem. Rev.* **95** 69
[11] Liu H, Ma H T, Li X Z, Li W Z, Wu M and Bao X H 2003 *Chemosphere* **50** 39
[12] Zheng Z, Huang B, Lu J, Wang Z, Qin X, Zhang X, Dai Y and Whangbo M-H 2012 *Chem. Commun.* **48** 5733
[13] Chen X, Liu L, Peter Y Y and Mao S S 2011 *Science* **331** 746
[14] Nowotny M K, Sheppard L R, Bak T and Nowotny J 2008 *J. Phys. Chem.* **112** 5275
[15] Pan X and Xu Y-J 2013 *J. Phys. Chem.* **117** 17996
[16] Pan X, Yang M-Q, Fu X, Zhang N and Xu Y-J 2013 *Nanoscale* **5** 3601
[17] Naldoni A, Allieta M, Santangelo S, Marelli M, Fabbri F, Cappelli S, Bianchi C L, Psaro R and Dal Santo V 2012 *J. Am. Chem. Soc.* **134** 7600
[18] Nitta A, Takase M, Takashima M, Murakami N and Ohtani B 2016 *Chem. Commun.* **52** 12096
[19] Rahimi N, Pax R and Gray E M 2019 *Prog. Solid State Chem.* **55** 1
[20] Lang D V 1974 *J. Appl. Phys.* **45** 3023
[21] Arcadipane E *et al* 2016 *RSC Adv.* **6** 55490
[22] Duckworth C, Brinkman A and Woods J 1983 *Phys. Status Solidi* A **75** K99
[23] Zimmermann C, Bonkerud J, Herklotz F, Sky T, Hupfer A, Monakhov E, Svensson B and Vines L 2018 *J. Appl. Phys.* **123** 161572
[24] Bonkerud J, Zimmermann C, Herklotz F, Weiser P M, Aarholt T, Verhoeven E F, Vines L and Monakhov E V 2020 *Mater. Res. Express* **7** 065903
[25] Float-zone-grown r-TiO_2 from MTI Corporation 2019 (https://www.mtixtl.com/tio2substrates.aspx (Accessed: 2019-12-05))
[26] Bogomolov V and Mirlin D 1968 *Phys. Status Solidi* b **27** 443
[27] Breckenridge R and Hosler W 1953 *Phys. Rev.* **91** 793
[28] Johnson O, Ohlsen W and Kingsbury P Jr 1968 *Phys. Rev.* **175** 1102

[29] Khomenko V, Langer K, Rager H and Fett A 1998 *Phys. Chem. Miner.* **25** 338
[30] Cronemeyer D 1959 *Phys. Rev.* **113** 1222
[31] Valigi M, Cordischi D, Minelli G, Natale P, Porta P and Keijzers C 1988 *J. Solid State Chem.* **77** 255
[32] Porter V, White W and Roy R 1972 *J. Solid State Chem.* **4** 250
[33] Verneuil-grown r-TiO_2 from Shinkosha 2019 (https://www.shinkosha.com/english/sehin/2_03.html (Accessed: 2019-12-05))
[34] Blood P and Orton J 1992 *The Electrical Characterization of Semiconductors: Majority Carriers and Electron States Academic* vol 13 Techniques of Physics (New York: Academic)
[35] van der Pauw L 1958 *Philips Tech. Rev.* **20** 220
[36] Herklotz F, Lavrov E and Weber J 2011 *Phys. Rev.* B **83** 235202
[37] Johnson O, DeFord J and Shaner J 1973 *J. Appl. Phys.* **44** 3008
[38] Rhoderick E and Williams R 1988 *Metal-Semiconductor Contacts* Monographs in electrical and electronic engineering (Oxford: Clarendon)
[39] Bonkerud J, Zimmermann C, Weiser P, Vines L and Monakhov E 2021 Determining the dielectric constant of rutile TiO_2 from implanted H-profiles (in preparation)
[40] Parker R 1961 *Phys. Rev.* **124** 1719
[41] Svensson B G, Rydén K H and Lewerentz B M S 1989 *J. Appl. Phys.* **66** 1699
[42] Istratov A A, Vyvenko O F, Hieslmair H and Weber E R 1998 *Meas. Sci. Technol.* **9** 477
[43] Istratov A 1997 *J. Appl. Phys.* **82** 2965
[44] Zimmermann C, Frodason Y K, Rønning V, Varley J B and Vines L 2020 *New J. Phys.* **22** 063033
[45] Weber J, Lavrov E and Herklotz F 2012 *Physica* B **407** 1456
[46] Shimomura K, Kadono R, Koda A, Nishiyama K and Mihara M 2015 *Phys. Rev.* B **92** 075203
[47] Weiser P M, Zimmermann C, Bonkerud J, Vines L and Monakhov E V 2020 *J. Appl. Phys.* **128** 145701
[48] Rahimi N, Pax R A and Gray E M 2016 *Prog. Solid State Chem.* **44** 86
[49] Henderson M A 1999 *Surf. Sci.* **419** 174
[50] Qiu J, Li S, Gray E, Liu H, Gu Q-F, Sun C, Lai C, Zhao H and Zhang S 2014 *J. Phys. Chem.* **118** 8824
[51] Haerudin H, Bertel S and Kramer R 1998 *J. Chem. Soc. Faraday Trans.* **94** 1481
[52] Deák P, Aradi B and Frauenheim T 2015 *Phys. Rev.* B **92** 045204
[53] Wickramaratne D, Dreyer C E, Monserrat B, Shen J-X, Lyons J L, Alkauskas A and Van de Walle C G 2018 *Appl. Phys. Lett.* **113** 192106